Solid-state NMR reveals a comprehensive view of the dynamics of the flexible, disordered N-terminal domain of amyloid-β fibrils

Received for publication, November 3, 2018, and in revised form, February 8, 2019 Published, Papers in Press, February 8, 2019, DOI 10.1074/jbc.RA118.006559

Dan Fai Au[‡], Dmitry Ostrovsky[§], Riqiang Fu[¶], and Liliya Vugmeyster[‡1]

From the Departments of [‡]Chemistry and [§]Mathematics, University of Colorado, Denver, Colorado 80204 and [¶]National High Field Magnetic Laboratory, Tallahassee, Florida 32310

Edited by Paul E. Fraser

Amyloid fibril deposits observed in Alzheimer's disease comprise amyloid-β (Aβ) protein possessing a structured hydrophobic core and a disordered N-terminal domain (residues 1–16). The internal flexibility of the disordered domain is likely essential for Aβ aggregation. Here, we used ^{2}H static solid-state NMR methods to probe the dynamics of selected side chains of the N-terminal domain of Aβ_{1-40} fibrils. Line shape and relaxation data suggested a two-state model in which the domain's free state undergoes a diffusive motion that is quenched in the bound state, likely because of transient interactions with the structured C-terminal domain. At 37 °C, we observed freezing of the dynamics progressively along the Aβ sequence, with the fraction of the bound state increasing and the rate of diffusion decreasing. We also found that without solvation, the diffusive motion is quenched. The solvent acted as a plasticizer reminiscent of its role in the onset of global dynamics in globular proteins. As the temperature was lowered, the fraction of the bound state exhibited sigmoidal behavior. The midpoint of the freezing curve coincided with the bulk solvent freezing for the N-terminal residues and increased further along the sequence. Using ^{2}H $R_{1\rho}$ measurements, we determined the conformational exchange rate constant between the free and bound states under physiological conditions. Zinc-induced aggregation leads to the enhancement of the dynamics, manifested by the faster conformational exchange, faster diffusion, and lower freezing-curve midpoints.

Amyloid-β (Aβ)[2] protein is one of the major components of neurotoxic amyloid plaques in the brains of patients with Alzheimer's disease. The deposits are made up of Aβ fibrils displaying distinct morphological features (1, 2). Aβ is also present *in vivo* in oligomeric form, which is believed to be very toxic and capable of disrupting the cell membrane (3, 4). Short fibrillary entities are also capable of membrane disruption, and, in general, cellular toxicity might be related to the dynamic properties of all Aβ species (5, 6).

Aβ_{1-40} is most abundant in fibrils, although Aβ_{1-42} is often considered to be more toxic (7). Aβ comprises a structured C-terminal domain spanning the well-characterized cross-β motif and a mostly unstructured N-terminal domain, corresponding to residues 1–16 of the full-length protein. Molecular dynamics simulations suggest that the N-terminal domain is not entirely disordered but can sample turns and β-sheet structures (8–11).

The N-terminal domain has been found by several studies to be crucial in regulating the aggregation properties of Aβ (12–18). It contains the main binding and regulatory sites for interaction with metals (19–25) as well as several regulatory sites that have recently been implicated to be controlled via post-translational modifications (16, 17, 26–29). For example, the H6R familial mutation associated with the early onset of Alzheimer's disease and isomerization of aspartate at position 7 to isoaspartate increase aggregation propensities and zinc-dependent oligomerization (26–30). *In vitro*, this type of isomerization has also been suggested to lead to enhanced insolubility and resistance to enzymatic degradation (26, 31–33). Furthermore, molecular dynamics simulations revealed differences in the correlated dynamics between the C-terminal and N-terminal domains upon mutations at positions 6 and 7, which are important for defining polymorphic states and are likely to be involved in altering the aggregation properties between the WT and mutants (9). In general, Hori *et al.* (35) hypothesized that the region around positions His-6 and Asp-7 can be a "hot spot" that facilitates Aβ deposition and the development of Alzheimer's disease (34). Another important regulatory spot in the N-terminal domain is likely to be related to the post-translational phosphorylation of Ser-8, which has been shown to lead to a distinctly different fibril morphology and suggested to affect the initial nucleation of Aβ fibrillation (27, 28) as well as promote and stabilize the formation of toxic aggregates (17, 36, 37).[3]

Animal models show that Zn^{2+} coordination can play a crucial role in the formation of plaques *in vivo* (20, 40, 41). At concentrations of the order of what is found at synapses, Zn^{2+}

This work was supported by National Institutes of Health Grant 1R15-GM111681 and National Science Foundation Grant 1726947. The authors declare that they have no conflicts of interest with the contents of this article. The content is solely the responsibility of the authors and does not necessarily represent the official views of the National Institutes of Health.
This article contains Figs. S1–S15 and supporting information SI1–SI11.

[1] To whom correspondence should be addressed: Dept. of Chemistry, University of Colorado, 1201 Laurimer St., Denver, CO 80204. E-mail: liliya.vugmeyster@ucdenver.edu.

[2] The abbreviations used are: Aβ, amyloid-β; TEM, transmission EM; Fmoc, fluorenylmethyloxycarbonyl; rad, radians; T, tesla(s); QCPMG, quadrupolar Carr–Purcell–Meiboom–Gill.

[3] Z. W. Hu, L. Vugmeyster, D. F. Au, D. Ostrovsky, Y. Sun, and W. Qiang, submitted for publication.

specifically binds to Aβ and promotes aggregation (42, 43). Noy *et al.* (44) proposed that Zn^{2+} stabilizes transient (nonfibrillary) amyloid forms. The concentration of zinc ions in amyloid plaques reaches 1 mM (43). Miller *et al.* (46) suggested that the mechanism of Zn^{2+} binding is due to a population shift of polymorphs, similar to other large zinc-binding proteins (47). In the NMR structure of Zn-bound $A\beta_{1-16}$ (48), His-6, Glu-11, His-13, and His-14 are coordinated with Zn. It has also been suggested that the aggregation may be governed by the conformational flexibility of His-6 (19).

The internal flexibility of the N-terminal domain is likely to be very important for its functionality of controlling the aggregation. Disordered protein regions are known for their control of multiple biological functions, including allosteric regulation and enzymatic catalysis (49–51). Combined with the high number of existing post-translational modifications and mutations in the N-terminal region, which have the potential to modify structural ensembles,[3] studies of the dynamics of this region can reveal the underlying molecular basis of the aggregation control associated with these modifications.

The general flexibility of noncore regions in Aβ has been demonstrated by multiple techniques such as nuclear magnetic resonance (NMR) (52–57), EPR (58), hydrogen-deuterium exchange probed by MS (59–61), X-ray crystallography (62), and fluorescence spectroscopy (63). However, experimental site-specific studies of the dynamics of the insoluble aggregates of Aβ in general and in the N-terminal domain in particular are relatively sparse due to challenges in obtaining the necessary resolution and sensitivity in the solid noncrystalline state (52, 64–69). Of note are the works of Fawzi *et al.* (70, 71), who utilized solution NMR saturation transfer approaches to probe the binding of monomeric Aβ to the surface of protofibrils.

In fact, the available structures of the WT $A\beta_{1-40}$ fibrils solved by solid-state NMR start at residue 9 (53, 72), highlighting the enhanced dynamics of the N-terminal region. Furthermore, Hong and co-workers (69) identified several pools of water in the fibrils such as in the matrix, interfibrillar, peptide-bound, and inside cavities. These different water pools are likely to be crucial in modulating the Aβ dynamics and transient interactions between the two domains. The structure of fibrils has been shown to be hydration-independent, at least in the structured region, based on chemical shift data (54). Thus, solvation likely has the largest effect on the properties of the dynamics rather than the overall structure. The motions in the N-terminal region in particular are expected to be highly sensitive to hydration.

The goal of this work was to characterize the site-specific dynamics of selected side chains in the flexible N-terminal domain in the context of hydrated $A\beta_{1-40}$ fibrils. We utilized deuterium static solid-state NMR techniques (73–76) in combination with the selective labeling of the side chains to achieve a comprehensive view of the dynamics of this largely disordered domain. The results allowed us to obtain a quantitative picture of the motions of the domain, with the flexibility of the side chains gradually decreasing along the N-terminal chain in the hydrated fibrils. Using ^2H $R_{1\rho}$ measurements, we also measured the rate of the conformational exchange of the N-terminal domain, which likely arises due to the transient interactions with the structured amyloid core. Finally, we compared the dynamics in the N-terminal domain of the mature $A\beta_{1-40}$ fibrils of the 3-fold symmetric polymorph with those of the amorphous aggregates formed in the presence of zinc, which demonstrate the enhancement of the dynamics.

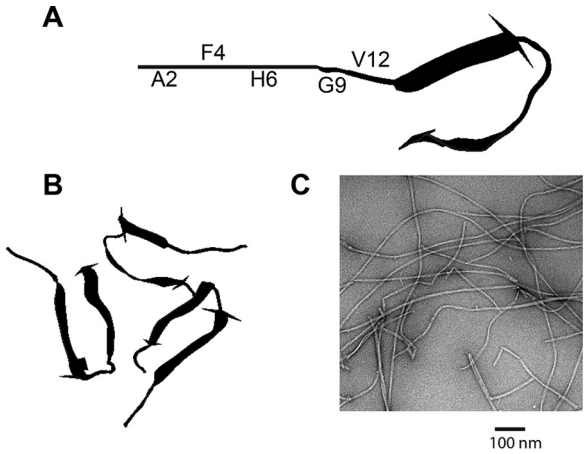

Figure 1. Schematic representation of $A\beta_{1-40}$ protein with the amino acid side chains probed in this work labeled. *A*, the structure of the monomer for residues 9 and beyond is taken from Protein Data Bank code 2LMP (77), whereas the rest of the N-terminal domain is shown schematically as a *line*. *B*, 3-fold symmetric fibril structure, top view (77). *C*, a typical negatively stained TEM image of the resulting morphology, shown for fibrils labeled at the Phe-4 site.

Results and discussion

"Singly" labeled samples for N-terminal domain side chains

Using $A\beta_{1-40}$ peptides with deuterium labels incorporated at a single residue along the N-terminal sequence, we generated a number of singly labeled samples of Aβ fibrils with morphologies corresponding mostly to the 3-folded symmetric/twisted polymorph (2, 67, 77). We employed previously developed protocols based on seeding procedures (2, 54) and confirmed the resulting morphologies using transmission EM (TEM).

The positions of the labeled residues and typical TEM images are shown in Fig. 1, and the position of the label in each individual side chain is listed in Table 1. For the His-6 side chain, the labeling with the τ–His modification was employed, for which the deuteration site is in the methyl group. This modification did not affect the morphology of the resulting fibrils (Fig. S1).

The deuterium line shape and longitudinal relaxation measurements were used to probe the dynamics in these selectively labeled samples. We have previously investigated the effect of multiple labeling sites in valine to investigate side-chain dynamics. The conclusion is that the relaxation times of C^β deuteron are over an order of magnitude longer than for methyl groups and are effectively suppressed in static experiments with the use of short interscan delays (78).

Qualitative analysis of the data suggests a hypothesis of free and transiently bound states for the N-terminal domain

The high-temperature line shapes for the N-terminal residues in the hydrated fibrils are significantly narrowed beyond what is expected due to typical local fluctuations such as fast methyl rotations, rotameric jumps, and ring flips (Fig. 2) (75,

Table 1
Residue-specific side-chain labeling patterns and main local motional modes at high temperatures for the free state of the N-terminal domain

Residue	Motional mode	Labeling pattern
Ala-2	Methyl three-site jumps	$-C^{\beta}D_3$
Phe-4	Ring flips	$-^{\beta}CH_2$–ring-d_5
His-6	Ring-flip high temperature limit (angle of 30.55° (between C^{β}–C^{γ} and CD_3–N^{ϵ}) (99) and methyl three-site jumps	$-^{\beta}CH_2$–ring-N–CD_3 (*i.e.* τ–His)
Gly-9	Two-site jumps of CD_2 with tetrahedral geometry	$-^{\alpha}CD_2$
Val-12	Methyl three-site jumps and rotameric interconversions	$-^{\beta}CD_2$–$(^{\gamma}CD_3)_2$

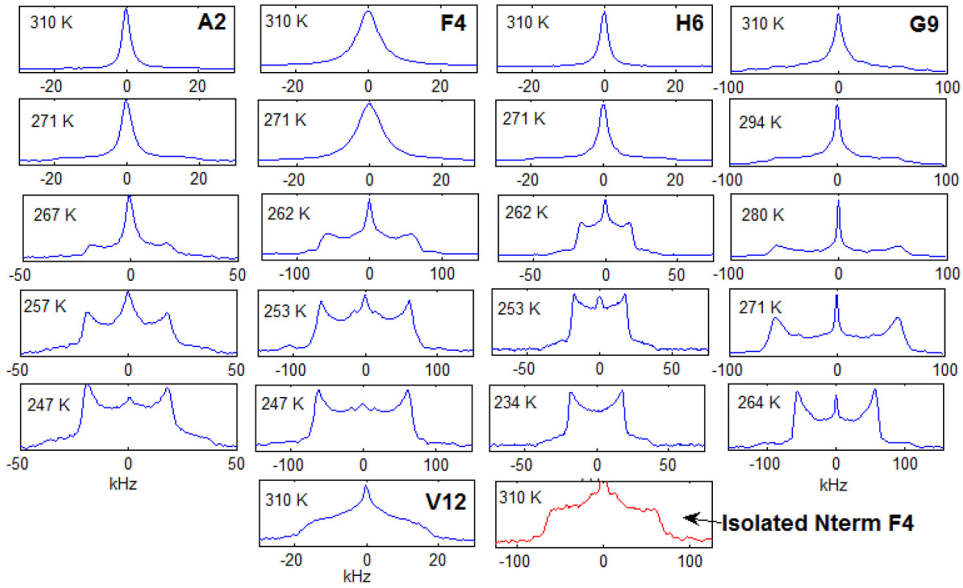

Figure 2. Representative ^{2}H static solid-state NMR line shape data in the hydrated fibril samples of $A\beta_{1-40}$ in the 3-fold symmetric polymorph at several temperatures. Also shown (*lowest right panel*, in *red*) is the line shape of the isolated N-terminal domain (residues 1–16) labeled at the F4-ring-d_5 position, for which the narrow peak around 0 kHz is attributed to the HOD signal. Note the intrinsic differences in the quadrupolar interactions for different residues, specified in Table 2.

79). As the temperature is lowered, a widening of the lines is observed with a sharp increase in the wide component appearing around the bulk freezing point of water (~265 K) for the Ala-2, Phe-4, and His-6 residues. For the Gly-9 and Val-12 residues, a significant fraction of the wide component is already apparent at much higher temperatures. For Val-12, a typical relatively wide pattern corresponding to rotameric jumps is observed at 37 °C, whereas for Gly-9 in addition to the wide component, there is still a narrowed region at the center of the spectrum. In addition, for the Phe-4, His-6, and Gly-9 side chains, the longitudinal relaxation data (Fig. 3) display a striking crossover curve (*i.e.* an abrupt sigmoidal-like change in T_1 with temperature), suggesting two different contributions to relaxation stemming from the dramatic differences in the local environments of the two components. At the same time, the relaxation curves remain single exponential even at the middle of the crossover (Figs. S2 and S3), pointing to the likelihood of exchange between the two components on the timescale faster than T_1. As will be elaborated later, for Ala-2 and Val-12, relaxation is dominated by fast local methyl rotations and is not sensitive to hydration.

The temperature-dependence behavior of both the line shapes and relaxation does not exhibit any hysteresis behavior; *i.e.* the same results are obtained independently of whether the experiments are performed by starting at the physiological conditions and freezing the samples or by starting at low temperatures and heating the samples. This points toward the fact that the system is in equilibrium with respect to freezing the bulk water surrounding the immediate hydration layer and cavities (69); in other words, we do not have a situation in which there are two states of bulk water.

Specific evidence on a dynamic exchange between the two fractions, detected by line shape and longitudinal measurements, is also seen from the rotating frame relaxation measurements, ^{2}H $R_{1\rho}$. These experiments are particularly sensitive to microsecond timescale conformational exchange processes (80–92). The existence of the relaxation rate "dispersion curve," the dependence of the relaxation rate on the radio frequency field strength, serves as an indication of the presence of conformational exchange at the microsecond timescale. As elaborated below, we observed such a dispersion profile for the fibrils labeled at the Ala-2 methyl position. Interestingly, for all residues, the dry fibrils lack the features of the narrowing behavior in the line shapes and the crossover behavior in the relaxation data (Figs. 3 and 4), indicating that solvation is crucial in the onset of the global dynamical modes responsible for these features.

Based on all the available data, we propose a hypothesis that in the hydrated fibrils, the N-terminal domain exchanges between the free state in which large-scale concerted motions of the whole domain dominate the dynamics at high temperatures and the "bound" state in which these motions are quenched (Fig. 5). The nature of the bound state is likely due to transient interactions with the well-structured C-terminal

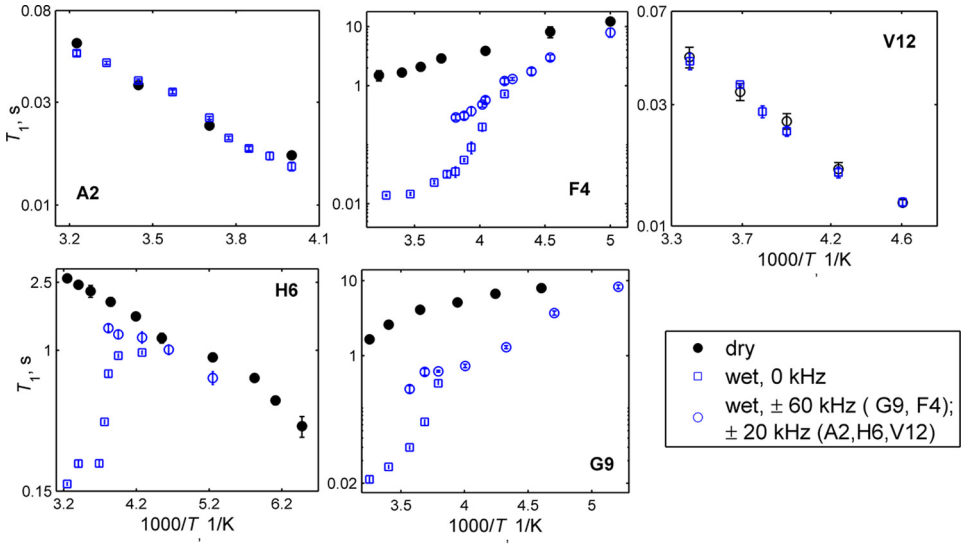

Figure 3. ^{2}H longitudinal relaxation times T_1 *versus* 1000/T recorded at 17.6-T field strength in the dry (*black*) and hydrated (*blue*) fibril samples of Aβ_{1-40} for the major singularities of the powder pattern spectra: 0 kHz (*squares*), ±20 kHz for Ala-2, His-6, and Val-12 (*circles*), and ±60 kHz for Phe-4 and Gly-9 (*circles*). *Error bars* smaller than the size of the *symbol* are not shown. Note the different T_1 scales for the different residues. *Error bars* shown represent the S.E. of the fits of the decay curves.

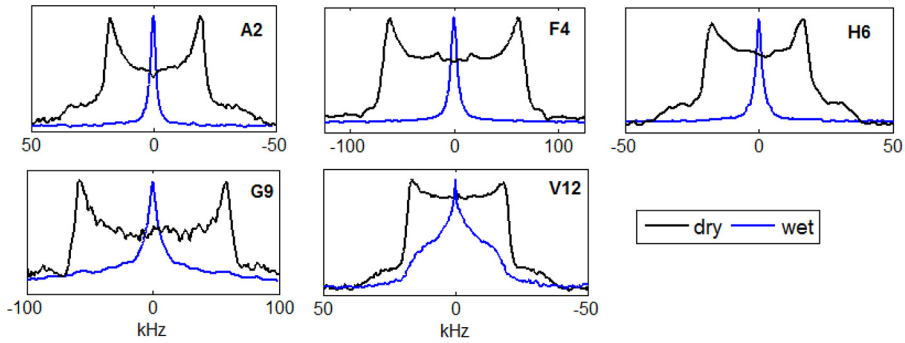

Figure 4. Comparison of the normalized ^{2}H static solid-state NMR line shapes for the dry (*black*) and hydrated (*blue*) states of the Aβ_{1-40} fibrils in the 3-fold symmetric polymorph.

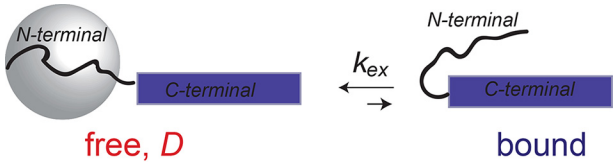

Figure 5. Schematic representation of the model in which the disordered N-terminal domain (*curved line*) transiently interacts with the structured C-terminal domain (*blue rectangle*). In the free state, the N-terminal domain is assumed to undergo isotropic diffusion, as represented by the *gray sphere*, whereas in the bound state, the interactions quench this mode. The parameters of the models are shown as the corresponding symbols.

domain of Aβ. Residues located closer to the N terminus (Ala-2, Phe-4, and His-6) have a significantly lower fraction of the bound state, probably due to weaker interactions with the C-terminal domain compared with the residues further along the chain. As the temperature is lowered, the large-scale motions of the N-terminal domain diminish, and they are very significantly quenched near the bulk freezing point of water when the frozen bulk solvent no longer acts as a plasticizer. This effect of water is reminiscent of the hydration effect on slow dynamics in globular proteins (*i.e.* solvent-driven glass transition) (78, 93–96). Bauer *et al.* (97) also reported the crucial effect of solvation on the μs–ms-scale dynamics of the exposed residues of amyloid fibrils composed of HET-s$_{218-289}$ protein using ^{13}C and ^{1}H solid-state NMR under magic-angle spinning conditions and over a broad temperature range. The role of solvent on amyloid structure formation has also been probed by explicit molecular dynamics simulations to illustrate how water controls the self-assembly of higher-order structures and plays a role in amyloid polymorphism (98). The rest of the quantitative data analysis proceeds according to the described hypothesis, and the $R_{1\rho}$ measurements allow us to determine the chemical exchange rate constant between the free and bound states under physiological conditions.

Note that the N-terminal domain in isolation (corresponding to residues 1–16 of the full-length Aβ) in the hydrated state surprisingly does *not* show the line narrowing observed in the context of the fibrils. Fig. 2 (see the *red line* in the *bottom panel*) demonstrates the line shape of this isolated fragment labeled at the F4-ring-d_5 position. Thus, it appears that the packing of the fibrils renders enhanced flexibility to the N-terminal domain, which likely is functionally relevant. It is also important to note that the methyl-bearing side chains in the C-terminal core of the fibrils (Leu-17, Leu-34, and Val-36), when probed with the same technique of ^{2}H line shape analysis, did not show any dependence on solvation, unlike the side chain of Met-35 span-

ning a water-accessible cavity (66, 67, 69). Thus, solvation in conjunction with the environment of the fibrils promotes the flexibility of the N-terminal domain. Without the environment of the fibrils in the lyophilized hydrated state, the side chains of the N-terminal fragment are free to stack against each other by forming nonnative intermolecular contacts, which are likely to lead to the partially aggregated state responsible for the observed restriction in the dynamics.

Determination of the fraction of free and bound states from the line shape data

The general strategy for the determination of the fractions of the free and bound states corresponds to the decomposition of the line shapes into a narrow component of the Lorentzian shape and the wide non-Lorentzian components (Fig. S4). The former component is assumed to correspond to the free state with motions governed by isotropic diffusion, and the latter component is assumed to correspond to the bound state. For the case of Gly-9, this analysis yielded an unreasonably high fraction of the bound state (75%) at 37 °C, which contradicted the existence of the cross-over in the relaxation data. Thus, for this residue, we assumed that a part of the non-Lorentzian line shape is due to deviations from isotropic diffusion. The deviation could arise because the probe is at the backbone. The fraction bound in this case was taken as a percentage of the rigid (full powder pattern) line shape. In this regard, it is important to note that for Val-12, located further along the backbone, all of the non-Lorentzian line shape can be attributed to the bound state, with some extent of rotameric motions of the valine side chains present in the bound state, as detailed under "Experimental procedures."

To determine to what extent the location of the probe on the backbone rather than on the side chain affects the freezing of Gly-9 at a higher temperature, we also probed the Phe-4 site at the backbone position labeled as D^{α} only (Fig. S5). The spectrum remains almost entirely unfrozen at 280 K, at which Gly-9 is already over 70% in the bound state. At 263 K, there is still a significant fraction of the mobile phase for the F4-D^{α} site. Thus, it is clear that the backbone position alone does not cause a significantly higher freezing point. Due to the low sensitivity of this sample (only one deuterium per Aβ molecule), quantitative line shape decomposition was unreliable, and we were not able to assess deviations from the approximation of isotropic tumbling.

The resulting fractions at 37 °C (Fig. 6*A*) show that the population of the bound state progressively increases along the N-terminal sequence. The temperature dependence of the populations (Fig. 6*B*) displays sigmoidal behavior. The data were fitted to the following function,

$$p_{\text{bound}} = a + \frac{b - a}{1 + \exp\left(\frac{T - T_m}{\sigma}\right)} \qquad \text{(Eq. 1)}$$

in which T_m is the midpoint of the freezing curve, σ is the characteristic width of the transition region, and a and b are the higher and lower temperature baselines, respectively. The midpoint of the transition is at 268 K for Ala-2, Phe-4, and His-6 and at 284 K for Gly-9 (supporting information SI5). Thus, the midpoint of the freezing of the first 6–7 residues coincide with the freezing of the bulk point of water, whereas for the residues further along the chain, freezing is observed at higher temperatures.

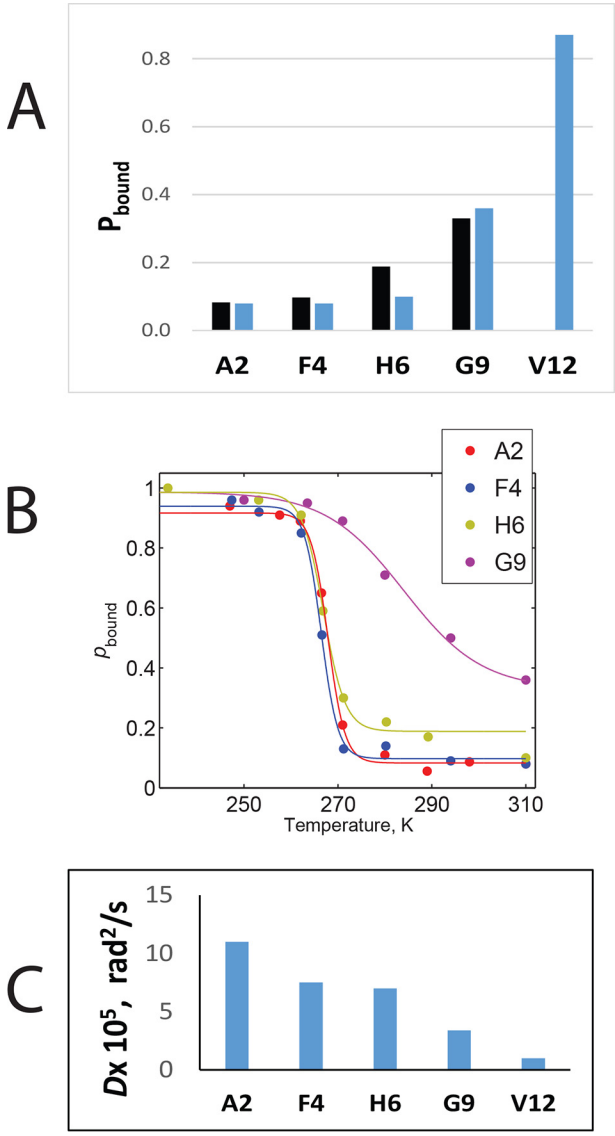

Figure 6. *A*, fraction of the bound state (p_{bound}) derived from the ^{2}H line shape analysis, either determined directly from line shape data at 37 °C (*blue*) or as the upper temperature baseline parameter from the fits to the sigmoidal curves of Equation 1 (*black*). Note that the fit to Equation 1 was not performed for Val-12. *B*, p_{bound} as a function of the temperature. The *solid lines* represent the fits to the data according to Equation 1. *C*, diffusion coefficient *D* fitted based on the ^{2}H line shapes at 37 °C according to the isotropic diffusion approximation.

Additionally, the transition is significantly wider for Gly-9 (the value of σ is 3.5–4 times higher than that of Ala-2–His-6) Note that parameter a might yield a more accurate overall high-temperature fraction bound projection than just the estimation at a single temperature of +37 °C, and we thus display it in the same figure (Fig. 6*A*) for comparison purposes.

Determination of the timescale of the large-scale motions in the free state assuming an isotropic diffusion model

We invoke the simplest assumption for the large-scale motions of the N-terminal domain as isotropic diffusion. Obvi-

ously, this is an approximation, as the environment in the fibrils is not expected to be isotropic. However, this simple model allows us to obtain the relative timescales of the diffusive motions in the free state. The local motional modes were taken as typical modes for the given residues consistent with the temperature dependence of the line shapes (73, 75, 79, 99, 100) (Table 1). By modeling isotropic diffusion as discrete nearest-neighbor jumps on the surface of a sphere, as described under "Experimental procedures," the diffusion coefficients D were obtained by matching the experimental and simulated line shapes. The resulting values of the diffusion coefficients at 37 °C are shown in Fig. 6*C*, and they demonstrate a sizeable decrease along the N-terminal sequence. An alternative model with the sharp temperature dependence of the diffusion coefficient could not reproduce the line shapes at temperatures close to T_m; *i.e.* it is not possible to reproduce the existence of both the central sharp component and the wide powder pattern (supporting information SI7 and Fig. S6) with a single value of D.

The origin of the crossover in relaxation curves and determination of the timescale of chemical exchange between free and bound states at temperatures close to the midpoint transition

The relaxation behavior (Fig. 3) both below and above freezing is governed by mechanisms consistent with the topology of the side chain (73, 79). Furthermore, the most effective mechanisms are closest in timescale to the Larmor precession frequencies: for the Ala-2 and Val-12 side chains, these are methyl three-site jumps; for Phe-4, the phenylalanine ring flips; and for Gly-9, these are two-site jumps of the CD_2 group. The situation is more complex for His-6 as in principle both fast methyl rotations and ring flips can contribute to relaxation. An interesting and important feature is that for the side chains for which there is a considerable hydration dependence of the relaxation (*i.e.* relaxation times become much smaller upon hydration), there is also a crossover in the relaxation curves. This is the case for the Phe-4, His-6, and Gly-9 side chains.

For the Phe-4 site, relaxation at high temperatures is consistent with ring flips, whereas at the low temperatures, the flipping motion slows significantly. Note that the diffusion around the ring rotation axis (*i.e.* around the χ_2 dihedral angle) is ruled out based on the line shape pattern (101, 102). At low temperatures, one can observe strong relaxation anisotropy: at a frequency of 0 kHz, the contribution is primarily from the free state, whereas at ±60 kHz, the contribution is primarily from the more rigid bound state. Around the midpoint of the crossover, when there is still a significant fraction of the free state even though the intrinsic relaxation rate of the bound state is not very effective, the relaxation of the wide component (±60 kHz) is actually governed by the exchange between the free and bound states, as elaborated at the end of this section.

For His-6, at low temperatures, the comparison with the dry sample in which methyl jumps dominate the relaxation as well as the analysis of the temperature dependence of the relaxation indicates that methyl three-site jumps are the main relaxation mechanism. The values of T_1 in the low temperature range of the relaxation curve show a decrease in temperature, indicating that the motions are in the fast regime with respect to the Larmor frequency. This behavior would not be expected for the ring-flipping motions of the imidazole ring. In contrast, at high temperatures, there is the onset of an additional ring-flipping motion of the imidazole ring, giving rise to a major contribution at a frequency of 0 kHz. The ring flipping of imidazole can be functionally relevant for the modulation of the metal coordination properties of the N-terminal domain. Similar to the case of Phe-4, at intermediate temperatures, the relaxation of the bound component is governed by the exchange between the free and bound states. However, unlike the case of Phe-4, the powder pattern spectrum of the bound state is motionally narrowed by ⅓ due to methyl rotations, and thus there is less of a spectral separation between the bound and free states, which complicates the determination of the exchange rates.

For the case of Gly-9, the two-site jumps of the CD_2 group are the major relaxation mechanism at both extremes of the temperature ranges, albeit with different efficiencies for the free and bound states. For the intermediate temperature range of 280–260 K, if we assume that the relaxation is determined by the CD_2 jumps in the bound state, the resulting rate constants would yield a line shape pattern inconsistent with the experimental results (*i.e.* these simulations would show overpronounced horns for the wide component). Thus, the exchange between the bound and free states again dominates the relaxation in this temperature range.

The quantitative details of the modeling of the relaxation rates are elaborated under "Experimental procedures." The temperature dependence of the rate constants and high and low temperature limits yield values of activation energies for the local motions. They do not provide any major insights relevant to our global picture, and we list them in supporting information SI6.

Based on the simplified treatment using the McConnell equations (103, 104), the relaxation of the bound state at intermediate temperatures for Gly-9, His-6, and Phe-4 is given by $R_1^{\text{bound}} = p_{\text{free}} k_{\text{ex}}$. By taking p_{free} from the line shape data, we calculate the k_{ex} rate for temperatures close to the midpoint of the relaxation crossover. These temperatures are slightly below the T_m values corresponding to the p_{bound} freezing curves from the line shape analysis (Fig. 7). The resulting values of k_{ex} are 21 ± 3 s^{-1} for Phe-4 at 262 K, 9 ± 2 s^{-1} for His-6 at 262 K, and 8 ± 2 s^{-1} for Gly-9 at 280 K.

Determination of the conformational exchange rate constant between bound and free states at 37 °C at the A2-CD_3 site using ^2H $R_{1\rho}$ measurements

To determine the rate of conformational exchange between the free and bound states of the N-terminal domain of the fibrils, we utilize ^2H solid-state NMR rotating frame relaxation dispersion measurements under static conditions, which we have previously tested using a model compound (105). Rotating frame NMR relaxation has yielded a multitude of insights into protein dynamics in solution (106), and the momentum has picked up to enhance the development of these techniques for solid-state applications (81–92).

^2H relaxation rates were measured as a function of the spin-locking field strengths, ω_{SL}, between 5 and 35 kHz (Fig. 7) for

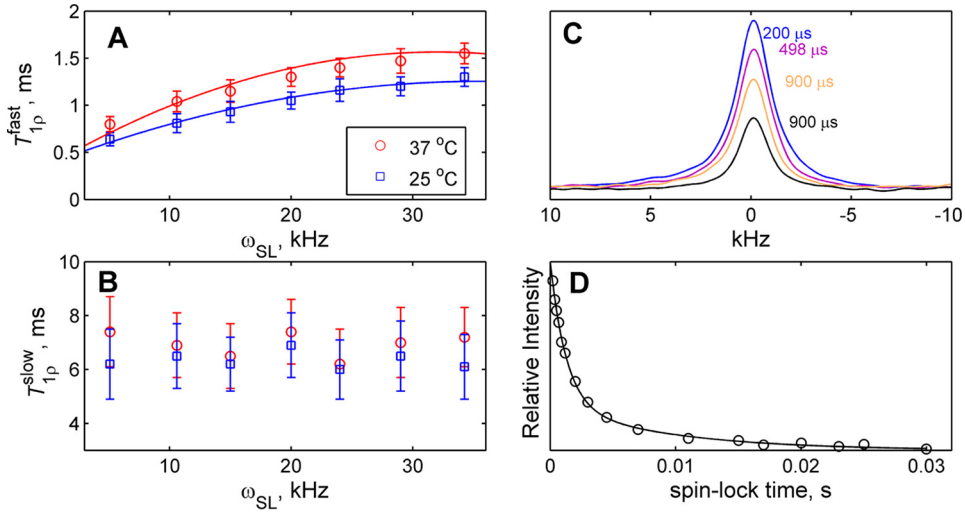

Figure 7. *A* and *B*, experimental ^{2}H $T_{1\rho}^{fast} = 1/R_{1\rho}^{fast}$ relaxation times (corresponding to the fast component of the double-exponential fit) (*A*) and $T_{1\rho}^{slow}$ *versus* spin-lock field ω_{SL} (*B*) at 37 (*red circles*) and 25 °C (*blue squares*) at 14 T for hydrated Aβ_{1-40} fibrils in the 3-fold symmetric polymorph labeled at the A2-C$^{\beta}$D$_3$ position. *Solid lines* represent the best-fit simulated data to the two-site exchange model described in the text. *C*, examples of the partially relaxed line shapes at 37 °C for the $R_{1\rho}$ measurements at several values of spin-lock times for the 15-kHz spin-lock field, indicated on the graph. *D*, experimental magnetization decay curves for the 15-kHz field at 37 °C. Peak intensities integrated over the −1 to +1-kHz region (which is approximately the width at the half-height of the peak shown in *C*) are in arbitrary units *versus* time (*circles*); the *solid line* shows the double-exponential fit. *Error bars* shown represent the S.E. of the fits of the decay curves.

the fibrils labeled at the A2-C$^{\beta}$D$_3$ position. Because of the significant narrowing of the line shapes due to the diffusive motion (Fig. 2), the analysis can be performed within the Redfield limit of NMR relaxation theory, given by the condition that the relaxation rate is much smaller than the rate constant of the underlying motional process (supporting information SI8) (107). Experimental relaxation decay curves are not exponential and can be approximated with a double-exponential decay (Fig. 7*D*), in which only the fast component (Fig. 7*A*) shows dependence on ω_{SL}. The slow component, with a relative contribution to overall signal intensity of 30%, is defined with a much smaller extent of precision within which it does not exhibit any pronounced dependence on ω_{SL} and is of the order of 6–7 ms.

Based on the line shape analysis, the fraction of the bound state is 8% for A2 at 37 °C (Fig. 6*A*) and the dynamics can be approximated by an isotropic diffusion model. In the bound state, the tensor is considered to be static with an effective quadrupolar coupling constant of 55 kHz after narrowing due to methyl rotations taken into account. The diffusion mode alone cannot explain the characteristic dependence of the fast component on ω_{SL} (SI8 and Fig. S7). Thus, the mode of the conformational exchange between the free and bound states plays a central role in defining the dispersion curve. The main fitting parameter for this mode is rate constant $k_{ex} = k_1 + k_{-1}$. The modeling procedure takes into account all possible relative tensor orientations in the free and bound states. Fitting the fast component ($T_{1\rho}^{fast} = 1/R_{1\rho}^{fast}$) of the double-exponential fit in this manner, one can thus extract the values of D and k_{ex}. The best-fitted values are $D = 3.5{\cdot}10^6$ rad^2/s and $k_{ex} = 3{\cdot}10^4$ s^{-1} (Fig. S8). The diffusion coefficient is larger than that determined solely from the line shape analysis, $1.1{\cdot}10^6$ rad^2/s.

The line width is very sensitive to the presence of slight motional anisotropy, and thus this deviation allows us to estimate its extent (supporting information SI8, Fig. S9, and supporting information SI10). As elaborated on in supporting information SI8 (Figs. S7–S12), the presence of the additional slow component points to the need for a more involved motional model with a possibility of including an additional state. It is interesting that an intermediate state was found for the exchange between the monomeric Aβ and its oligomer-bound form, even for the methyl group of Ala-2, based on dark-state exchange saturation transfer (DEST) solution NMR measurements (70, 71).

To probe the temperature dependence of the conformational exchange process, we also performed the measurements at the lower temperature of 25 °C (Fig. 7*A*). The fitted value of k_{ex} is unchanged ($3{\cdot}10^4$ s^{-1}) within the precision of the data, whereas the diffusion coefficient is smaller, $D = 2.5{\cdot}10^6$ s^{-1}, and the fraction of the bound state is 9%. Thus, the results suggest a relatively low activation energy value for the conformational exchange process between the bound and free states.

Zinc-induced aggregation leads to the enhancement of the dynamics

To determine whether the dynamics are sensitive to different states of Aβ, we investigated the aggregates formed in the presence of equimolar amounts of zinc chloride. These amorphous aggregates have a very wide range of sizes from 1,000 to 10,000 nm, as estimated from dynamic light scattering results. The observed distribution is in qualitative agreement with that found by Noy *et al.* (44) for zinc-containing aggregates based on analytical ultracentrifugation studies. In particular, they emphasized the existence of large-molecular-weight aggregates in a very broad range of sizes. The details of the dynamic light scattering and TEM data are shown in supporting information SI11 (Figs. S14 and S15). Thus, the sample morphology is different from the fibrillary form.

We analyzed these aggregates using the ^{2}H static line shapes and $R_{1\rho}$ measurements employed for the fibrillary form (Fig. 8).

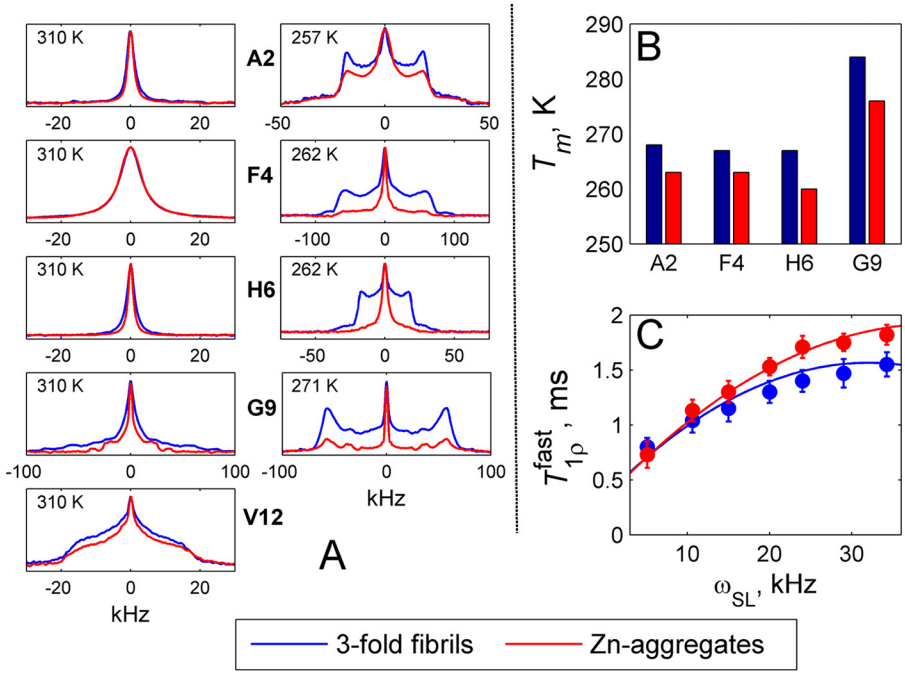

Figure 8. Comparison of the dynamics between the hydrated 3-fold Aβ_{1-40} fibrils (*blue*) and hydrated Zn^{2+}-induced aggregates. *A*, ^{2}H static solid-state NMR line shapes at 37 °C and representative spectra around the freezing transition region. *B*, midpoint melting temperatures T_m derived from fitting the fractions of the bound states (supporting information SI10) to Equation 1. *C*, ^{2}H $T_{1\rho}^{fast}$ relaxation times (corresponding to the fast component of the double-exponential fit) *versus* the spin-lock field ω_{SL} at 37 °C at 14 T for the A2-C$^{\beta}$D$_3$ site. *Solid lines* represent the best-fit simulated data to the two-site exchange model described in the text. *Error bars* shown represent the S.E. of the fits of the decay curves.

At 37 °C, there are minor changes in the spectra with an overall moderate extent of narrowing compared with the fibrillary form (Fig. 8*A*), with more pronounced changes toward the end of the N terminus (His-6, Gly-9, and Val-12). Upon freezing, it is evident that the midpoint of the freezing curves is shifted to lower temperatures (see Fig. S13 and the typical spectra close to the midpoint of freezing in Fig. 8*a*). Fitting the freezing curves to Equation 1 indicates a significant lowering of the midpoint temperatures (Fig. 8*B*, supporting information SI5, and Fig. S13) by about 4–5 K for Ala-2 and Phe-4 and 7–8 K for His-6 and Gly-9. Additionally, the value of σ for Gly-9 is about 40% smaller, reflecting the narrowing of the transition. It has previously been suggested that the aggregation may be partially controlled by the conformational flexibility of His-6 (19). Our results indicate that the changes in the dynamics in the presence of zinc are more pronounced for the side chain of His-6 and further residues along the backbone of the N-terminal domain, which correlates with the previous study of Istrate *et al.* (19). We note that the use of τ–His reduces the coordination efficiency of the histidine ring, and thus the actual changes in the dynamics upon zinc-induced aggregation may be even more pronounced.

The ^{2}H $R_{1\rho}$ measurements (Fig. 8*C*) at the A2-CD$_3$ site display a steeper dispersion for the fast component of the relaxation curve $T_{1\rho}^{fast}$. The fraction of the bound state based on the line shape analysis is 6% for this residue compared with 8% for the fibrils. The fitted values of the conformational exchange constant within the model of Fig. 5 is $4.5{\cdot}10^4$ s^{-1}, which is 1.5 times larger than that for the fibrillary form, and the fitted value of the diffusion coefficient D is $5{\cdot}10^6$ rad^2/s compared with $3.5{\cdot}10^6$ rad^2/s in the 3-fold symmetric fibrils. The combined results of the line shapes and $R_{1\rho}$ relaxation analysis indicate the enhanced mobility of the aggregates.

As mentioned in the Introduction, the flexibility of the N-terminal domain of Aβ and its exposure to solvent has been known for some time (52, 54, 56, 57). In particular, the works of Olofsson *et al.* (56) and Whittemore *et al.* (57) have measured hydrogen-deuterium exchange rates for backbone amide hydrogen in solution using solution NMR spectroscopy. Compared with the structured regions, the N-terminal domain displayed low protection factors for several of the residues that could be detected. The current work expands these results to the fibrillary state of Aβ in the 3-fold polymorph and shows a clear progression for the freezing of the dynamics along the sequence in terms of both the fraction of the bound state and the kinetics of the motions approximated by the isotropic diffusion mode. Furthermore, instead of the backbone, the side chains were tackled, which is expected to be important in the inter-residue contacts (both intra- and intermolecular) that can hinder flexibility. Additionally, the ^{2}H $R_{1\rho}$ experiments allowed us to identify the conformational exchange rate constant, likely due to the transient interactions between the unstructured N terminus and core of the fibrils.

As a first step toward assessing changes in the dynamics in different forms of Aβ, we determined the differences between the 3-fold symmetric fibrillary form and Zn-induced aggregates. To obtain the full biological significance of the role of the dynamics in the potential control of aggregation, further studies will need to focus on discerning the changes in the dynamics between different polymorphs of Aβ (1, 2, 77, 108–110) as well as in the variants of Aβ that include post-translational modifications in the N terminus and mutations mentioned in the

Introduction. In particular, it will be important to test the 2-fold native polymorph as well as H6R and D7N mutants (11, 35, 111) and the Ser-8–phosphorylated fibrils that were shown to lead to conformational changes in the N terminus and accelerate aggregation (17, 27, 28).

Conclusion

Our results demonstrate the quantitative features of the flexibility in the N-terminal domain of Aβ fibrils probed at several selectively deuterated side-chain sites along the N-terminal sequences. Based on deuterium static solid-state line shape and relaxation data, we proposed the two-state model in which the free state of the N-terminal domain undergoes a diffusive motion; however, in the bound state, this motion is quenched, likely due to transient interaction with the structured C-terminal subdomain. Local motions such as rotameric jumps, methyl rotations, and ring flips dominate the dynamics of the bound state, whereas they coexist with the diffusive motion in the free state.

The fraction of the bound state at the physiological temperature was determined to be 8% for the most extreme N-terminal residues (Ala-2, His-4, and Phe-6), and this increases significantly further along the sequence, with Gly-9 already at 36% and Val-12 at 87%. We also calculated the rate of the diffusive motion by using the isotropic diffusion approximation that, although an oversimplification, allows us to obtain the relative scale of the diffusive motion along the sequence. Thus, the diffusion coefficient of His-6 is 64% of that of Ala-2, but it drops to 30% for Gly-9 and to under 10% for Val-12.

The temperature dependence of the fractions exhibits sigmoidal behavior, with the midpoint of freezing at 267–268 K for Ala-2, Phe-4, and His-6 and at 284 K for Gly-9. Thus, the midpoint of the freezing of the first 6–7 residues is close to the temperature of the freezing of the bulk water, whereas for residues further along the chain, freezing is observed at higher temperatures. The crossover in the longitudinal relaxation times is also evident for the residues that display strong solvation dependence of the relaxation: Phe-4, His-6, and Gly-9. For Ala-2 and Val-12, the relaxation is dominated by local methyl rotations. Around the midpoint of the crossover in the relaxation curves, relaxation in the bound state is governed primarily by the exchange process between the two states, and thus we can determine the exchange rate constant between the free and bound states at these conditions. The rate constant falls by about 21 s^{-1} for Phe-4 (at 262 K) and 9 s^{-1} for His-6 (at 262 K) and Gly-9 (at 280 K).

The newly developed ^2H $R_{1\rho}$ methodology permitted the determination of the conformational exchange rate constant between the free and bound states at the physiological temperature. Probed at the A2-CD_3 site, the conformational exchange rate constant is $3{\cdot}10^4$ s^{-1}. The effect of zinc-induced aggregation on the dynamics manifests in the overall enhancement of the dynamics. The conformational exchange rate constant is increased by a factor of 1.5, and the line shapes are somewhat narrowed at room temperature, especially for the His-6, Gly-9, and Val-12 residues. Furthermore, the midpoint of the freezing curves is lowered by 4–5 K for Ala-2 and Phe-4 and by 7–8 K for His-6 and Gly-9. Future studies of the different polymorphs of Aβ as well as mutants and post-translational modifications at the N-terminal region will be helpful for revealing the biological importance of the flexibility of this disordered domain.

Experimental procedures

Preparation of the $A\beta_{1-40}$ peptide

The peptide was prepared by using solid-state peptide synthesis (performed by Thermo Fisher Scientific, Rockford, IL). Fluorenylmethyloxycarbonyl (Fmoc)-phenylalanine-ring-d_5, Fmoc-alanine-d_3, Fmoc-glycine-d_2, and Fmoc-histidine-ring-CD_3 were purchased from Cambridge Isotopes Laboratories (Andover, MA). The native sequence is DAEFRHDSGYEVHHQKLVFFAEDVGSNKGAIIGLMVGGVV. The peptides were purified by reversed-phase HPLC, and their identity and purity were confirmed by MS and reversed-phase HPLC. The resulting peptides had isotopic labels in only one chosen residue. The details of the labeling patterns are shown in Table 1.

Preparation of the fibrils

Fibrils of the WT $A\beta_{1-40}$ in the "twisted/3-fold" polymorphs were produced by using established seeded growth protocols under quiescent conditions (2, 54). For the preparation of the bulk samples, lyophilized peptides were initially dissolved at a 5 mM concentration in dimethyl sulfoxide (DMSO) and immediately transferred to a solution of 10 mM monosodium phosphate buffer at pH 7.4 also containing seeds in a 1:10 ratio by weight. The fibrils were allowed to grow for at least 4 days at room temperature with sonication performed at 24 h during the growth period: aliquots corresponding to 10% of the bulk volume were taken out of solution and sonicated for 2 min by using a probe sonicator, cooled for 15 min, and then added back into the bulk solution. The peptide concentration of the bulk samples was 0.5 mg/ml. The bulk fibrils were pelleted by centrifuging at 300,000 × *g* for 12 h. Fibril pellets were resuspended in deionized water, rapidly frozen with liquid nitrogen, and lyophilized. The resulting morphologies were confirmed with TEM imaging (Fig. 1 and supporting information SI1).

Preparation of amorphous aggregates in the presence of zinc

Lyophilized peptides were dissolved at a 5 mM concentration in DMSO and immediately transferred to a solution of 10 mM monosodium phosphate buffer containing equimolar amounts of zinc chloride at pH 7.4 to a total concentration of peptide of 0.5 mg/ml. The aggregates were allowed to grow for at least 3 days at room temperature. The solution underwent dialysis in water using a membrane with a 3-kDa molecular-mass cutoff followed by lyophilization.

Transmission electron microscopy

Samples were stored at room temperature and diluted to about 0.1 mg/ml with Millipore filtered water. Samples were negatively stained by using the drop method (112) in the following manner. Four-microliter aliquots of the sample, Millipore filtered water, and 2% uranyl acetate aqueous stain were applied sequentially to a freshly glow-discharged (113) Formvar carbon–coated 300 mesh copper grid for the fol-

Table 2
Quadrupolar coupling tensor parameters: quadrupolar coupling constant C_q and asymmetry η for the N-terminal residues of $A\beta_{1-40}$

Residue	Effective C_q and η in the fast motional limit for line shape simulations	Static C_q and η for relaxation simulations
Ala-2	C_q = 55.5 kHz, η = 0	C_q = 165.5kHz, η = 0
Phe-4	C_q = 107 kHz, η = 0.7	C_q = 180kHz, η = 0
His-6	C_q = 32.5kHz, η = 0.63	C_q = 159 kHz, η = 0
Gly-9	C_q = 77.6 kHz, η = 1	C_q = 155 kHz, η = 0
Val-12	C_q = 53.3 kHz, η = 0 and rotameric interconversions	C_q = 160 kHz, η = 0

lowing incubation times: 2 min, 10 s, and 1.5 min, respectively. Each 4-μl droplet was removed by wicking with filter paper for 5 s. The filter paper was blotted prior to the addition of the next droplet. After staining, the grid was air-dried under a vacuum for 20 min. Images were collected under low-dose conditions of 120,000× using an FEI Tecnai G2 Spirit Biotwin microscope operating at 80 kV.

Hydration and preparation of the NMR samples

A hydrated state with a water content of 200% by weight was achieved by exposing lyophilized powder to water vapor in a sealed chamber at 25 °C until the water content reached saturation levels corresponding to about 40% by weight (24–48 h was sufficient to achieve this) followed by pipetting the remaining water by using deuterium-depleted H_2O. The samples were packed in 5-mm NMR tubes (cut to 21-mm length) using Teflon tape to center the sample volume in the coil of the NMR probe. The amount of material packed was 12–15 mg for Ala- and Val-labeled peptides and 20–28 mg for His-, Phe-, and Gly-labeled peptides.

Deuteron static solid-state NMR spectroscopy

Experiments were performed on 17.6- and 14.1-T spectrometers equipped with a static probe operating at temperatures between 160 and 380 K. Line shape experiments were performed with a quadrupole echo pulse sequence based on an eight-step phase cycle (73) with a delay of 31 μs between 90° pulses. A line broadening function of 0.5–2 kHz was chosen to enhance the signal. T_1 measurements under static conditions were performed at 17. 6 T by using the inversion recovery sequence for relaxation times below 80 ms and a saturation recovery sequence for longer times. For the relaxation measurements at low temperatures at which the full-width powder pattern was observed, we utilized the multiple echo acquisition detection scheme (QCPMG) for signal enhancement (114). Briefly, QCPMG detection breaks the powder pattern spectrum into a series of spikes that roughly follow the shape of the powder pattern. Unlike magic-angle spinning, QCPMG detection does not suppress relaxation anisotropy (115). The durations of 90° pulses were between 2.0 and 3.0 μs. Ten to 15 QCPMG echoes were collected with 52-μs pulse spacing, corresponding to QCPMG spikelets (side bands) spaced at 20-kHz intervals. The number of scans ranged from 128 to 2,048 depending on the signal-to-noise ratio in each sample. Five to seven relaxation delays were collected. Relaxation times T_1 were obtained by using single-exponential fits to the magnetization buildup curves.

The $R_{1\rho}$ experiment was performed as described in previous work (105) with the pulse sequence (Fig. S12) and further details shown in supporting information SI8. A 600-MHz NMR spectrometer with a Bruker Neo console equipped with a wide-line low-E probe (116) with a 5-mm-inner-diameter coil was employed. Spin-lock times varied between 200 μs and 30 ms (12–17 relaxation delays), and powers varied from 5 to 35 kHz. Sixteen to 32 dummy scans were utilized.

Motional modeling

The isotropic diffusion of the free state was modeled as discrete nearest-neighbor jumps on the surface of a sphere, using 192 sites with the DistMesh program (38) for the discretization of the Smoluchowski equation. The jump rate was the same for all pairs of sites and was selected to match the second nonzero eigenvalue of the diffusion operator (corresponding to the second-order Legendre polynomial eigenfunction) to be 6D. Supporting information SI7 provides further details of line shape modeling. The parameters of the quadrupolar tensors, quadrupolar coupling constant C_q, and tensor asymmetry η (73) for each type or residue were taken from the low-temperature spectra. The effective values in the fast motional regime, given by the limit at which the rate constant is much greater than C_q, were calculated for the free state by employing the motional models described under "Results." The values are listed in Table 2. For the case of Gly-9, the averaging of the tensor in the fast limit results in an asymmetry parameter of 1, which yields effective narrowing by itself without the diffusion mode. Diffusion causes further line shape narrowing. In the case of valine-d_3, the additional local mode of rotameric jumps had to be added explicitly as the fast limit approximation was not valid. At 37 °C, the rotameric exchange rate constant of 1×10^5 s^{-1} and three rotamers, as well as the corresponding rotations around the χ_1 angle, with populations in the 5:1:1 ratio were used. The simulations utilized the EXPRESS program (39). For the simulated line shapes, an additional line broadening of 1–1.5 kHz was used to approximately account for the effect of inhomogeneous dipolar interactions (45).

To model the longitudinal relaxation rates, static quadrupolar tensor parameters were used (Table 2), and the motional modes listed in Table 1 under "Results and discussion" were assumed. The values of the rate constants were obtained by matching the experimental and simulated values of T_1. The activation energies in the high and low temperature limits were determined by using the Arrhenius law for the rate constants.

To model the $R_{1\rho}$ rates, in addition to the isotropic diffusion mode modeled as described for the line shapes, an additional mode of exchange between the free and bound states was included. This was accomplished by the introduction of one additional site with an arbitrary fixed angular position in the crystal-fixed frame. The exchange was modeled by jumps between every site describing the spherical diffusion and

bound-state site (supporting information SI8). These simulations were performed in the Redfield framework (107).

Author contributions—D. F. A. and L. V. investigation; D. F. A., D. O., R. F., and L. V. methodology; D. O. and L. V. conceptualization; D. O. software; D. O. and L. V. validation; D. O. visualization; D. O., R. F., and L. V. writing-review and editing; L. V. data curation; L. V. formal analysis; L. V. supervision; L. V. funding acquisition; L. V. writing-original draft; L. V. project administration; D. F. A. sample preparation; D. O. molecular modeling.

Acknowledgments—Some of the experiments were performed at the National High Magnetic Field Laboratory, which is supported by National Science Foundation (NSF) Cooperative Agreement NSF/DMR-1644779, the State of Florida, and the United States Department of Energy. We also acknowledge Alex Greenwood for technical assistance at the William and Mary NMR facility, a resource jointly managed by the Departments of Applied Science and Physics.

References

1. Paravastu, A. K., Qahwash, I., Leapman, R. D., Meredith, S. C., and Tycko, R. (2009) Seeded growth of β-amyloid fibrils from Alzheimer's brain-derived fibrils produces a distinct fibril structure. *Proc. Natl. Acad. Sci. U.S.A.* **106,** 7443–7448 CrossRef Medline
2. Petkova, A. T., Leapman, R. D., Guo, Z., Yau, W. M., Mattson, M. P., and Tycko, R. (2005) Self-propagating, molecular-level polymorphism in Alzheimer's β-amyloid fibrils. *Science* **307,** 262–265 CrossRef Medline
3. Serra-Vidal, B., Pujadas, L., Rossi, D., Soriano, E., Madurga, S., and Carulla, N. (2014) Hydrogen/deuterium exchange-protected oligomers populated during Aβ fibril formation correlate with neuronal cell death. *ACS Chem. Biol.* **9,** 2678–2685 CrossRef Medline
4. Laganowsky, A., Liu, C., Sawaya, M. R., Whitelegge, J. P., Park, J., Zhao, M., Pensalfini, A., Soriaga, A. B., Landau, M., Teng, P. K., Cascio, D., Glabe, C., and Eisenberg, D. (2012) Atomic view of a toxic amyloid small oligomer. *Science* **335,** 1228–1231 CrossRef Medline
5. Delgado, D. A., Doherty, K., Cheng, Q., Kim, H., Xu, D., Dong, H., Grewer, C., and Qiang, W. (2016) Distinct membrane disruption pathways are induced by 40-residue β-amyloid peptides. *J. Biol. Chem.* **291,** 12233–12244 CrossRef Medline
6. Hubin, E., van Nuland, N. A., Broersen, K., and Pauwels, K. (2014) Transient dynamics of Aβ contribute to toxicity in Alzheimer's disease. *Cell. Mol. Life Sci.* **71,** 3507–3521 CrossRef Medline
7. Jarrett, J. T., Berger, E. P., and Lansbury, P. T., Jr. (1993) The C-terminus of the β protein is critical in amyloidogenesis. *Ann. N. Y. Acad. Sci.* **695,** 144–148 CrossRef Medline
8. Yang, M., and Teplow, D. B. (2008) Amyloid β-protein monomer folding. *J. Mol. Biol.* **384,** 450–464 CrossRef Medline
9. Xu, L., Chen, Y., and Wang, X. (2014) Dual effects of familial Alzheimer's disease mutations (D7H, D7N, and H6R) on amyloid β peptide: correlation dynamics and zinc binding. *Proteins* **82,** 3286–3297 CrossRef Medline
10. Sgourakis, N. G., Yan, Y., McCallum, S. A., Wang, C., and Garcia, A. E. (2007) The Alzheimer's peptides Aβ 40 and 42 adopt distinct conformations in water: a combined MD/NMR study. *J. Mol. Biol.* **368,** 1448–1457 CrossRef Medline
11. Ono, K., Condron, M. M., and Teplow, D. B. (2010) Effects of the English (H6R) and Tottori (D7N) familial Alzheimer disease mutations on amyloid β-protein assembly and toxicity. *J. Biol. Chem.* **285,** 23186–23197 CrossRef Medline
12. Mazzitelli, S., Filipello, F., Rasile, M., Lauranzano, E., Starvaggi-Cucuzza, C., Tamborini, M., Pozzi, D., Barajon, I., Giorgino, T., Natalello, A., and Matteoli, M. (2016) Amyloid-β 1–24 C-terminal truncated fragment promotes amyloid-β 1–42 aggregate formation in the healthy brain. *Acta Neuropathol. Commun.* **4,** 110 CrossRef Medline
13. Brännström, K., Öhman, A., Nilsson, L., Pihl, M., Sandblad, L., and Olofsson, A. (2014) The N-terminal region of amyloid β controls the aggregation rate and fibril stability at low pH through a gain of function mechanism. *J. Am. Chem. Soc.* **136,** 10956–10964 CrossRef Medline
14. Morris, C., Cupples, S., Kent, T. W., Elbassal, E. A., Wojcikiewicz, E. P., Yi, P., and Du, D. (2018) N-terminal charged residues of amyloid-β peptide modulate amyloidogenesis and interaction with lipid membrane. *Chemistry* **24,** 9494–9498 CrossRef Medline
15. Nussbaum, J. M., Schilling, S., Cynis, H., Silva, A., Swanson, E., Wangsanut, T., Tayler, K., Wiltgen, B., Hatami, A., Rönicke, R., Reymann, K., Hutter-Paier, B., Alexandru, A., Jagla, W., Graubner, S., *et al.* (2012) Prion-like behaviour and tau-dependent cytotoxicity of pyroglutamylated amyloid-β. *Nature* **485,** 651–655 CrossRef Medline
16. Kummer, M. P., Hermes, M., Delekarte, A., Hammerschmidt, T., Kumar, S., Terwel, D., Walter, J., Pape, H. C., König, S., Roeber, S., Jessen, F., Klockgether, T., Korte, M., and Heneka, M. T. (2011) Nitration of tyrosine 10 critically enhances amyloid β aggregation and plaque formation. *Neuron* **71,** 833–844 CrossRef Medline
17. Rezaei-Ghaleh, N., Amininasab, M., Kumar, S., Walter, J., and Zweckstetter, M. (2016) Phosphorylation modifies the molecular stability of β-amyloid deposits. *Nat. Commun.* **7,** 11359 CrossRef Medline
18. Xu, L., Nussinov, R., and Ma, B. (2016) Allosteric stabilization of the amyloid-β peptide hairpin by the fluctuating N-terminal. *Chem. Commun.* **52,** 1733–1736 CrossRef Medline
19. Istrate, A. N., Kozin, S. A., Zhokhov, S. S., Mantsyzov, A. B., Kechko, O. I., Pastore, A., Makarov, A. A., and Polshakov, V. I. (2016) Interplay of histidine residues of the Alzheimer's disease Aβ peptide governs its Zn-induced oligomerization. *Sci. Rep.* **6,** 21734 CrossRef Medline
20. Bush, A. I. (2013) The metal theory of Alzheimer's disease. *J. Alzheimers Dis.* **33,** Suppl. 1, S277–S281 CrossRef Medline
21. Miller, Y., Ma, B. Y., and Nussinov, R. (2012) Metal binding sites in amyloid oligomers: complexes and mechanisms. *Coord. Chem. Rev.* **256,** 2245–2252 CrossRef
22. Tõugu, V., Tiiman, A., and Palumaa, P. (2011) Interactions of Zn(II) and Cu(II) ions with Alzheimer's amyloid-β peptide. Metal ion binding, contribution to fibrillization and toxicity. *Metallomics* **3,** 250–261 CrossRef Medline
23. Miura, T., Yoda, M., Tsutsumi, C., Murayama, K., and Takeuchi, H. (2010) Conformational regulation of amyloid β-peptide by lipid membranes and metal ions. *Yakugaku Zasshi* **130,** 495–501 CrossRef Medline
24. Miura, T., Suzuki, K., Kohata, N., and Takeuchi, H. (2000) Metal binding modes of Alzheimer's amyloid β-peptide in insoluble aggregates and soluble complexes. *Biochemistry* **39,** 7024–7031 CrossRef Medline
25. Kulikova, A. A., Makarov, A. A., and Kozin, S. A. (2015) Roles of zinc ions and structural polymorphism of β-amyloid in the development of Alzheimer's disease. *Mol. Biol.* **49,** 217–230 CrossRef
26. Kummer, M. P., and Heneka, M. T. (2014) Truncated and modified amyloid-β species. *Alzheimers Res. Ther.* **6,** 28 CrossRef Medline
27. Rezaei-Ghaleh, N., Kumar, S., Walter, J., and Zweckstetter, M. (2016) Phosphorylation interferes with maturation of amyloid-β fibrillar structure in the N terminus. *J. Biol. Chem.* **291,** 16059–16067 CrossRef Medline
28. Hu, Z.-W., Ma, M.-R., Chen, Y.-X., Zhao, Y.-F., Qiang, W., and Li, Y.-M. (2017) Phosphorylation at Ser^8 as an intrinsic regulatory switch to regulate the morphologies and structures of Alzheimer's 40-residue β-amyloid (Aβ40) fibrils. *J. Biol. Chem.* **292,** 2611–2623 CrossRef Medline
29. Jawhar, S., Wirths, O., and Bayer, T. A. (2011) Pyroglutamate amyloid-β (Aβ): a hatchet man in Alzheimer disease. *J. Biol. Chem.* **286,** 38825–38832 CrossRef Medline
30. Roher, A. E., Lowenson, J. D., Clarke, S., Wolkow, C., Wang, R., Cotter, R. J., Reardon, I. M., Zürcher-Neely, H. A., Heinrikson, R. L., Ball, M. J., and Greenberg, B. D. (1993) Structural alterations in the peptide backbone of β-amyloid core protein may account for its deposition and stability in Alzheimer's disease. *J. Biol. Chem.* **268,** 3072–3083 Medline
31. Shimizu, T., Fukuda, H., Murayama, S., Izumiyama, N., and Shirasawa, T. (2002) Isoaspartate formation at position 23 of amyloid β peptide enhanced fibril formation and deposited onto senile plaques and vascular amyloids in Alzheimer's disease. *J. Neurosci. Res.* **70,** 451–461 CrossRef Medline

32. Kuo, Y. M., Webster, S., Emmerling, M. R., De Lima, N., and Roher, A. E. (1998) Irreversible dimerization/tetramerization and post-translational modifications inhibit proteolytic degradation of Aβ peptides of Alzheimer's disease. *Biochim. Biophys. Acta* **1406,** 291–298 CrossRef Medline
33. Fukuda, H., Shimizu, T., Nakajima, M., Mori, H., and Shirasawa, T. (1999) Synthesis, aggregation, and neurotoxicity of the Alzheimer's Aβ 1–42 amyloid peptide and its isoaspartyl isomers. *Bioorg. Med. Chem. Lett.* **9,** 953–956 CrossRef Medline
34. Janssen, J. C., Beck, J. A., Campbell, T. A., Dickinson, A., Fox, N. C., Harvey, R. J., Houlden, H., Rossor, M. N., and Collinge, J. (2003) Early onset familial Alzheimer's disease—mutation frequency in 31 families. *Neurology* **60,** 235–239 CrossRef Medline
35. Hori, Y., Hashimoto, T., Wakutani, Y., Urakami, K., Nakashima, K., Condron, M. M., Tsubuki, S., Saido, T. C., Teplow, D. B., and Iwatsubo, T. (2007) The Tottori (D7N) and English (H6R) familial Alzheimer disease mutations accelerate Aβ fibril formation without increasing protofibril formation. *J. Biol. Chem.* **282,** 4916–4923 CrossRef Medline
36. Kumar, S., and Walter, J. (2011) Phosphorylation of amyloid β (Aβ) peptides—a trigger for formation of toxic aggregates in Alzheimer's disease. *Aging* **3,** 803–812 CrossRef Medline
37. Kumar, S., Singh, S., Hinze, D., Josten, M., Sahl, H.-G., Siepmann, M., and Walter, J. (2012) Phosphorylation of amyloid-β peptide at serine 8 attenuates its clearance via insulin-degrading and angiotensin-converting enzymes. *J. Biol. Chem.* **287,** 8641–8651 CrossRef Medline
38. Persson, P.-O., and Strang, G. (2004) A simple mesh generator in MATLAB. *SIAM Rev.* **46,** 329–345 CrossRef
39. Vold, R. L., and Hoatson, G. L. (2009) Effects of jump dynamics on solid state nuclear magnetic resonance line shapes and spin relaxation times. *J. Magn. Reson.* **198,** 57–72 CrossRef Medline
40. Hamley, I. W. (2012) The amyloid β peptide: a chemist's perspective. Role in Alzheimer's and fibrillization. *Chem. Rev.* **112,** 5147–5192 CrossRef Medline
41. Ayton, S., Lei, P., and Bush, A. I. (2015) Biometals and their therapeutic implications in Alzheimer's disease. *Neurotherapeutics* **12,** 109–120 CrossRef Medline
42. Suh, S. W., Jensen, K. B., Jensen, M. S., Silva, D. S., Kesslak, P. J., Danscher, G., and Frederickson, C. J. (2000) Histochemically-reactive zinc in amyloid plaques, angiopathy, and degenerating neurons of Alzheimer's diseased brains. *Brain. Res.* **852,** 274–278 CrossRef Medline
43. Lovell, M. A., Robertson, J. D., Teesdale, W. J., Campbell, J. L., and Markesbery, W. R. (1998) Copper, iron and zinc in Alzheimer's disease senile plaques. *J. Neurol. Sci.* **158,** 47–52 CrossRef Medline
44. Noy, D., Solomonov, I., Sinkevich, O., Arad, T., Kjaer, K., and Sagi, I. (2008) Zinc-amyloid-β interactions on a millisecond time-scale stabilize non-fibrillar Alzheimer-related species. *J. Am. Chem. Soc.* **130,** 1376–1383 CrossRef Medline
45. Hirschinger, J., Miura, H., Gardner, K. H., and English, A. D. (1990) Segmental dynamics in the crystalline phase of nylon 66: solid-state ^{2}H NMR. *Macromolecules* **23,** 2153–2169 CrossRef
46. Miller, Y., Ma, B., and Nussinov, R. (2010) Zinc ions promote Alzheimer Aβ aggregation via population shift of polymorphic states. *Proc. Natl. Acad. Sci. U.S.A.* **107,** 9490–9495 CrossRef Medline
47. Iannuzzi, C., Adrover, M., Puglisi, R., Yan, R., Temussi, P. A., and Pastore, A. (2014) The role of zinc in the stability of the marginally stable IscU scaffold protein. *Protein Sci.* **23,** 1208–1219 CrossRef Medline
48. Tsvetkov, P. O., Kulikova, A. A., Golovin, A. V., Tkachev, Y. V., Archakov, A. I., Kozin, S. A., and Makarov, A. A. (2010) Minimal Zn^{2+} binding site of amyloid-β. *Biophys. J.* **99,** L84–L86 CrossRef Medline
49. Wright, P. E., and Dyson, H. J. (2015) Intrinsically disordered proteins in cellular signalling and regulation. *Nat. Rev. Mol. Cell Biol.* **16,** 18–29 CrossRef Medline
50. Berlow, R. B., Dyson, H. J., and Wright, P. E. (2018) Expanding the paradigm: intrinsically disordered proteins and allosteric regulation. *J. Mol. Biol.* **430,** 2309–2320 CrossRef Medline
51. Larion, M., Miller, B., and Brüschweiler, R. (2015) Conformational heterogeneity and intrinsic disorder in enzyme regulation: glucokinase as a case study. *Intrinsically Disord. Proteins* **3,** e1011008 CrossRef Medline
52. Scheidt, H. A., Morgado, I., Rothemund, S., and Huster, D. (2012) Dynamics of amyloid β fibrils revealed by solid-state NMR. *J. Biol. Chem.* **287,** 2017–2021 CrossRef Medline
53. Lührs, T., Ritter, C., Adrian, M., Riek-Loher, D., Bohrmann, B., Döbeli, H., Schubert, D., and Riek, R. (2005) 3D structure of Alzheimer's amyloid-β(1–42) fibrils. *Proc. Natl. Acad. Sci. U.S.A.* **102,** 17342–17347 CrossRef Medline
54. Petkova, A. T., Yau, W. M., and Tycko, R. (2006) Experimental constraints on quaternary structure in Alzheimer's β-amyloid fibrils. *Biochemistry* **45,** 498–512 CrossRef Medline
55. Bertini, I., Gonnelli, L., Luchinat, C., Mao, J., and Nesi, A. (2011) A new structural model of $Aβ_{40}$ fibrils. *J. Am. Chem. Soc.* **133,** 16013–16022 CrossRef Medline
56. Olofsson, A., Sauer-Eriksson, A. E., and Ohman, A. (2006) The solvent protection of Alzheimer amyloid-β-(1–42) fibrils as determined by solution NMR spectroscopy. *J. Biol. Chem.* **281,** 477–483 CrossRef Medline
57. Whittemore, N. A., Mishra, R., Kheterpal, I., Williams, A. D., Wetzel, R., and Serpersu, E. H. (2005) Hydrogen-deuterium (H/D) exchange mapping of Aβ(1–40) amyloid fibril secondary structure using nuclear magnetic resonance spectroscopy. *Biochemistry* **44,** 4434–4441 CrossRef Medline
58. Török, M., Milton, S., Kayed, R., Wu, P., McIntire, T., Glabe, C. G., and Langen, R. (2002) Structural and dynamic features of Alzheimer's Aβ peptide in amyloid fibrils studied by site-directed spin labeling. *J. Biol. Chem.* **277,** 40810–40815 CrossRef Medline
59. Kheterpal, I., Zhou, S., Cook, K. D., and Wetzel, R. (2000) Aβ amyloid fibrils possess a core structure highly resistant to hydrogen exchange. *Proc. Natl. Acad. Sci. U.S.A.* **97,** 13597–13601 CrossRef Medline
60. Wang, S. S., Tobler, S. A., Good, T. A., and Fernandez, E. J. (2003) Hydrogen exchange-mass spectrometry analysis of β-amyloid peptide structure. *Biochemistry* **42,** 9507–9514 CrossRef Medline
61. Kheterpal, I., Chen, M., Cook, K. D., and Wetzel, R. (2006) Structural differences in Aβ amyloid protofibrils and fibrils mapped by hydrogen exchange—mass spectrometry with on-line proteolytic fragmentation. *J. Mol. Biol.* **361,** 785–795 CrossRef Medline
62. Sawaya, M. R., Sambashivan, S., Nelson, R., Ivanova, M. I., Sievers, S. A., Apostol, M. I., Thompson, M. J., Balbirnie, M., Wiltzius, J. J., McFarlane, H. T., Madsen, A. Ø., Riekel, C., and Eisenberg, D. (2007) Atomic structures of amyloid cross-β spines reveal varied steric zippers. *Nature* **447,** 453–457 CrossRef Medline
63. Liu, H., Morris, C., Lantz, R., Kent, T. W., Elbassal, E. A., Wojcikiewicz, E. P., and Du, D. (2018) Residue-specific dynamics and local environmental changes in Aβ40 oligomer and fibril formation. *Angew. Chem. Int. Ed. Engl.* **57,** 8017–8021 CrossRef Medline
64. Linser, R., Sarkar, R., Krushelnitzky, A., Mainz, A., and Reif, B. (2014) Dynamics in the solid-state: perspectives for the investigation of amyloid aggregates, membrane proteins and soluble protein complexes. *J. Biomol. NMR* **59,** 1–14 CrossRef Medline
65. Vugmeyster, L., Ostrovsky, D., Hoatson, G. L., Qiang, W., and Falconer, I. B. (2017) Phenylalanine side-chain in the hydrophobic core of amyloid fibrils reveals a solvent-driven dynamical transition. *J. Phys. Chem. B* **121,** 7267–7275 CrossRef Medline
66. Vugmeyster, L., Ostrovsky, D., Clark, M. A., Falconer, I. B., Hoatson, G. L., and Qiang, W. (2016) Fast motions of key methyl groups in Amyloid-β fibrils. *Biophys. J.* **111,** 2135–2148 CrossRef Medline
67. Vugmeyster, L., Clark, M. A., Falconer, I. B., Ostrovsky, D., Gantz, D., Qiang, W., and Hoatson, G. L. (2016) Flexibility and solvation of amyloid-β hydrophobic core. *J. Biol. Chem.* **291,** 18484–18495 CrossRef Medline
68. Karamanos, T. K., Kalverda, A. P., Thompson, G. S., and Radford, S. E. (2015) Mechanisms of amyloid formation revealed by solution NMR. *Prog. Nucl. Magn. Reson. Spectrosc.* **88–89,** 86–104 CrossRef Medline
69. Wang, T., Jo, H., DeGrado, W. F., and Hong, M. (2017) Water distribution, dynamics, and interactions with Alzheimer's β-amyloid fibrils investigated by solid-state NMR. *J. Am. Chem. Soc.* **139,** 6242–6252 CrossRef Medline

70. Fawzi, N. L., Libich, D. S., Ying, J., Tugarinov, V., and Clore, G. M. (2014) Characterizing methyl-bearing side chain contacts and dynamics mediating amyloid β protofibril interactions using ^{13}C(methyl)-DEST and lifetime line broadening. *Angew. Chem. Int. Ed. Engl.* **53,** 10345–10349 CrossRef Medline
71. Fawzi, N. L., Ying, J., Ghirlando, R., Torchia, D. A., and Clore, G. M. (2011) Atomic-resolution dynamics on the surface of amyloid-β protofibrils probed by solution NMR. *Nature* **480,** 268–272 CrossRef Medline
72. Paravastu, A. K., Petkova, A. T., and Tycko, R. (2006) Polymorphic fibril formation by residues 10–40 of the Alzheimer's β-amyloid peptide. *Biophys. J.* **90,** 4618–4629 CrossRef Medline
73. Vold, R. L., and Vold, R. R. (1991) Deuterium relaxation in molecular solids, in *Advances in Magnetic and Optical Resonance* (Warren, W., ed) Vol. 16, pp. 85–171, Academic Press, San Diego, CA
74. Meints, G. A., Miller, P. A., Pederson, K., Shajani, Z., and Drobny, G. (2008) Solid-state nuclear magnetic resonance spectroscopy studies of furanose ring dynamics in the DNA HhaI binding site. *J. Am. Chem. Soc.* **130,** 7305–7314 CrossRef Medline
75. Vugmeyster, L., and Ostrovsky, D. (2017) Static solid-state ^{2}H NMR methods in studies of protein side-chain dynamics. *Prog. Nucl. Magn. Reson. Spectrosc.* **101,** 1–17 CrossRef Medline
76. Molugu, T. R., Lee, S., and Brown, M. F. (2017) Concepts and methods of solid-state NMR spectroscopy applied to biomembranes. *Chem. Rev.* **117,** 12087–12132 CrossRef Medline
77. Paravastu, A. K., Leapman, R. D., Yau, W. M., and Tycko, R. (2008) Molecular structural basis for polymorphism in Alzheimer's β-amyloid fibrils. *Proc. Natl. Acad. Sci. U.S.A.* **105,** 18349–18354 CrossRef Medline
78. Vugmeyster, L., Ostrovsky, D., Khadjinova, A., Ellden, J., Hoatson, G. L., and Vold, R. L. (2011) Slow motions in the hydrophobic core of chicken villin headpiece subdomain and their contributions to configurational entropy and heat capacity from solid-state deuteron NMR measurements. *Biochemistry* **50,** 10637–10646 CrossRef Medline
79. Vugmeyster, L., and Ostrovsky, D. (2018) Basic experiments in ^{2}H static NMR for the characterization of protein side-chain dynamics. *Methods* **148,** 136–145 CrossRef Medline
80. Palmer, A. G., 3rd (2004) NMR characterization of the dynamics of biomacromolecules. *Chem. Rev.* **104,** 3623–3640 CrossRef Medline
81. Lakomek, N.-A., Penzel, S., Lends, A., Cadalbert, R., Ernst, M., and Meier, B. H. (2017) Microsecond dynamics in ubiquitin probed by solid-state NMR ^{15}N R1ρ relaxation experiments under fast MAS (60–110 kHz). *Chemistry* **23,** 9425–9433 CrossRef Medline
82. Krushelnitsky, A., Zinkevich, T., Reif, B., and Saalwächter, K. (2014) Slow motions in microcrystalline proteins as observed by MAS-dependent ^{15}N rotating-frame NMR relaxation. *J. Magn. Reson.* **248,** 8–12 CrossRef Medline
83. Kurauskas, V., Izmailov, S. A., Rogacheva, O. N., Hessel, A., Ayala, I., Woodhouse, J., Shilova, A., Xue, Y., Yuwen, T., Coquelle, N., Colletier, J.-P., Skrynnikov, N. R., and Schanda, P. (2017) Slow conformational exchange and overall rocking motion in ubiquitin protein crystals. *Nat. Commun.* **8,** 145 CrossRef Medline
84. Quinn, C. M., and McDermott, A. E. (2009) Monitoring conformational dynamics with solid-state R1ρ experiments. *J. Biomol. NMR* **45,** 5–8 CrossRef Medline
85. Ma, P., Haller, J. D., Zajakala, J., Macek, P., Sivertsen, A. C., Willbold, D., Boisbouvier, J., and Schanda, P. (2014) Probing transient conformational states of proteins by solid-state R(1ρ) relaxation-dispersion NMR spectroscopy. *Angew. Chem. Int. Ed. Engl.* **53,** 4312–4317 CrossRef Medline
86. Quinn, C. M., and McDermott, A. E. (2012) Quantifying conformational dynamics using solid-state R1ρ experiments. *J. Magn. Reson.* **222,** 1–7 CrossRef Medline
87. Gauto, D. F., Hessel, A., Rovó, P., Kurauskas, V., Linser, R., and Schanda, P. (2017) Protein conformational dynamics studied by ^{15}N and ^{1}H R1ρ relaxation dispersion: application to wild-type and G53A ubiquitin crystals. *Solid State Nucl. Magn. Reson.* **87,** 86–95 CrossRef Medline
88. Rovó, P., and Linser, R. (2018) Microsecond timescale protein dynamics: a combined solid-state NMR Approach. *Chemphyschem* **19,** 34–39 CrossRef Medline
89. Rovó, P., and Linser, R. (2017) Microsecond time scale proton rotating-frame relaxation under magic angle spinning. *J. Phys. Chem. B* **121,** 6117–6130 CrossRef Medline
90. Krushelnitsky, A., Gauto, D., Rodriguez Camargo, D. C., Schanda, P., and Saalwächter, K. (2018) Microsecond motions probed by near-rotary-resonance R1ρ^{15}N MAS NMR experiments: the model case of protein overall-rocking in crystals. *J. Biomol. NMR* **71,** 53–67 CrossRef Medline
91. Shannon, M. D., Theint, T., Mukhopadhyay, D., Surewicz, K., Surewicz, W. K., Marion, D., Schanda, P., and Jaroniec, C. P. (2019) Conformational dynamics in the core of human Y145Stop prion protein amyloid probed by relaxation dispersion NMR. *Chemphyschem* **20,** 311–317 CrossRef Medline
92. Smith, A. A., Testori, E., Cadalbert, R., Meier, B. H., and Ernst, M. (2016) Characterization of fibril dynamics on three timescales by solid-state NMR. *J. Biomol. NMR* **65,** 171–191 CrossRef Medline
93. Doster, W. (2008) The dynamical transition of proteins, concepts and misconceptions. *Eur. Biophys. J.* **37,** 591–602 CrossRef Medline
94. Lewandowski, J. R., Halse, M. E., Blackledge, M., and Emsley, L. (2015) Direct observation of hierarchical protein dynamics. *Science* **348,** 578–581 CrossRef Medline
95. Ringe, D., and Petsko, G. A. (2003) The 'glass transition' in protein dynamics: what it is, why it occurs, and how to exploit it. *Biophys. Chem.* **105,** 667–680 CrossRef Medline
96. Kussell, E., and Shakhnovich, E. I. (2002) Glassy dynamics of side-chain ordering in a simple model of protein folding. *Phys. Rev. Lett.* **89,** 168101–168110 CrossRef Medline
97. Bauer, T., Dotta, C., Balacescu, L., Gath, J., Hunkeler, A., Böckmann, A., and Meier, B. H. (2017) Line-broadening in low-temperature solid-state NMR spectra of fibrils. *J. Biomol. NMR* **67,** 51–61 CrossRef Medline
98. Thirumalai, D., Reddy, G., and Straub, J. E. (2012) Role of water in protein aggregation and amyloid polymorphism. *Acc. Chem. Res* **45,** 83–92 CrossRef Medline
99. Malinska, M., Dauter, M., Kowiel, M., Jaskolski, M., and Dauter, Z. (2015) Protonation and geometry of histidine rings. *Acta Crystallogr. D Biol. Crystallogr.* **71,** 1444–1454 CrossRef Medline
100. Vold, R. R. (1994) Deuterium NMR studies of dynamics in solids and liquid crystals, in *Nuclear Magnetic Resonance Probes of Molecular Dynamics* (Tycko, R., ed) pp. 27–112, Kluwer Academic Publishers, Dordrecht, The Netherlands
101. Gall, C. M., Cross, T. A., DiVerdi, J. A., and Opella, S. J. (1982) Protein dynamics by solid-State NMR—aromatic rings of the coat protein in Fd bacteriophage. *Proc. Natl. Acad. Sci. U.S.A.* **79,** 101–105 CrossRef Medline
102. Hiyama, Y., Silverton, J. V., Torchia, D. A., Gerig, J. T., and Hammond, S. J. (1986) Molecular structure and dynamics of crystalline para-fluoro-D,L-phenylalanine—a combined X-ray NMR investigation. *J. Am. Chem. Soc.* **108,** 2715–2723 CrossRef
103. McConnell, H. M. (1958) Reaction rates by nuclear magnetic resonance. *J. Chem. Phys.* **28,** 430–431 CrossRef
104. Vugmeyster, L., Ostrovsky, D., Moses, M., Ford, J. J., Lipton, A. S., Hoatson, G. L., and Vold, R. L. (2010) Comparative dynamics of leucine methyl groups in FMOC-leucine and in a protein hydrophobic core probed by solid-state deuteron NMR over 7–324K temperature range. *J. Phys. Chem. B* **114,** 15799–15807 CrossRef Medline
105. Vugmeyster, L., and Ostrovsky, D. (2019) Deuterium rotating frame NMR relaxation measurements in the solid state under static conditions for quantification of dynamics. *Chemphyschem* **20,** 333–342 CrossRef Medline
106. Broersen, K., Rousseau, F., and Schymkowitz, J. (2010) The culprit behind amyloid β peptide related neurotoxicity in Alzheimer's disease: oligomer size or conformation? *Alzheimers Res. Ther.* **2,** 12 CrossRef Medline
107. Abragam, A. (1961) *Principles of Nuclear Magnetism*, Clarendon Press, Oxford
108. Hubin, E., Deroo, S., Schierle, G. K., Kaminski, C., Serpell, L., Subramaniam, V., van Nuland, N., Broersen, K., Raussens, V., and Sarroukh, R. (2015) Two distinct β-sheet structures in Italian-mutant amyloid-β fibrils: a potential link to different clinical phenotypes. *Cell. Mol. Life Sci.* **72,** 4899–4913 CrossRef Medline

109. Kodali, R., Williams, A. D., Chemuru, S., and Wetzel, R. (2010) Aβ(1–40) forms five distinct amyloid structures whose β-sheet contents and fibril stabilities are correlated. *J. Mol. Biol.* **401,** 503–517 CrossRef Medline
110. Meinhardt, J., Sachse, C., Hortschansky, P., Grigorieff, N., and Fändrich, M. (2009) Aβ(1–40) fibril polymorphism implies diverse interaction patterns in amyloid fibrils. *J. Mol. Biol.* **386,** 869–877 CrossRef Medline
111. Viet, M. H., Nguyen, P. H., Ngo, S. T., Li, M. S., and Derreumaux, P. (2013) Effect of the Tottori familial disease mutation (D7N) on the monomers and dimers of Aβ40 and Aβ42. *ACS Chem. Neurosci.* **4,** 1446–1457 CrossRef Medline
112. Harris, J. R., and Horne, J. W. (1991) Negative staining, in *Electron Microscopy in Biology* (Harris, J. R., ed) pp. 203–228, IRL Press, Oxford
113. Dubochet, J., Groom, M., and Mueller-Neuteboom, S. (1982) The mounting of macromolecules for electron microscopy with particular reference to surface phenomena and the treatment of support films by glow discharge, in *Advances in Optical and Electron Microscopy* (Barrer, R., and Cosslett, V. E., eds) Vol. 8, pp. 107–135, Elsevier, Amsterdam, The Netherlands
114. Larsen, F. H., Jakobsen, H. J., Ellis, P. D., and Nielsen, N. C. (1998) High-field QCPMG-MAS NMR of half-integer quadrupolar nuclei with large quadrupole couplings. *Mol. Phys.* **95,** 1185–1195 CrossRef
115. Vold, R. L., Hoatson, G. L., Vugmeyster, L., Ostrovsky, D., and De Castro, P. J. (2009) Solid state deuteron relaxation time anisotropy measured with multiple echo acquisition. *Phys. Chem. Chem. Phys.* **11,** 7008–7012 CrossRef Medline
116. Gor'kov, P. L., Chekmenev, E. Y., Li, C., Cotten, M., Buffy, J. J., Traaseth, N. J., Veglia, G., and Brey, W. W. (2007) Using low-E resonators to reduce RF heating in biological samples for static solid-state NMR up to 900 MHz. *J. Magn. Reson.* **185,** 77–93 CrossRef Medline

Solid-state NMR reveals a comprehensive view of the dynamics of the flexible, disordered N-terminal domain of amyloid- β fibrils

Dan Fai Au, Dmitry Ostrovsky, Riqiang Fu and Liliya Vugmeyster

J. Biol. Chem. 2019, 294:5840-5853.
doi: 10.1074/jbc.RA118.006559 originally published online February 8, 2019
